



# Immobilized particle coating for optimum photon and TiO<sub>2</sub> utilization in scaled air treatment photo reactors



Cristina S. Lugo-Vega<sup>a</sup>, Benito Serrano-Rosales<sup>b</sup>, Hugo de Lasa<sup>a,\*</sup>

<sup>a</sup> Chemical Reactor Engineering Centre (CREC), Faculty of Engineering Science, Department of Chemical And Biochemical Engineering, University of Western Ontario, London, Ontario, N6A 5B9, Canada

<sup>b</sup> Unidad Académica de Ciencias Químicas, Programa de Ingeniería Química, Universidad Autónoma de Zacatecas, 98000 Zacatecas, Campus UAZ Siglo XXI, 98168, Mexico

## ARTICLE INFO

### Article history:

Received 21 February 2016

Received in revised form 4 May 2016

Accepted 25 May 2016

Available online 27 May 2016

### Keywords:

Air treatment

Photocatalysis

VOC

Acetone

Quantum yield

TiO<sub>2</sub> immobilization methods

## ABSTRACT

This study reports the critical importance of the particle state in TiO<sub>2</sub> immobilized photocatalysis. To address this, TiO<sub>2</sub> coatings are prepared using two methods: an Air Assisted Spray with an Automatized Spinning Coating (TiO<sub>2</sub>-AAS-ASC) and a Spread Coating (TiO<sub>2</sub>-SCM). The state of the TiO<sub>2</sub> particles is investigated using SEM and local gravimetry. It is proven that the TiO<sub>2</sub>-AAS-ASC displays homogeneity, limited particle agglomeration, close to optimum thickness and stability under flow. Furthermore, the prepared coatings are evaluated in terms of photoactivity using acetone in air mineralization in the 24–49 μmol/L initial concentration range. This allows Quantum Efficiency evaluations based on absorbed photons and hydroxyl radical consumed. It is proven that the TiO<sub>2</sub>-AAS-ASC exhibits a close to expected optimum photoactivity and QYs in the 0.4–0.5 range. Furthermore, when the TiO<sub>2</sub>-AAS-ASC is assessed in terms of QY per unit weight of photocatalyst (QY/W), it shows a value 3 times higher than the TiO<sub>2</sub>-SCM. This high photon utilization is close to the best possible level expected for an optimized TiO<sub>2</sub> coating.

© 2016 Elsevier B.V. All rights reserved.

## 1. Introduction

People spend approximately 70–90% of their life inside [1,2]. As a result, indoor air pollution has been described as being one of most significant risk factors for some respiratory and heart diseases [3,4]. Among indoor air contaminants, volatile organic compounds (VOC) are found to be in high concentrations in enclosed spaces (1000 times more concentrated than outdoor air). Indoor VOCs are caused mainly by emissions of cleaning products, paints, furniture and building materials [5]. The high health risks of exposure to VOCs in indoor environments have led to the search for efficient VOC removal methods. Heterogeneous photocatalysis is a most valuable method for complete degradation of indoor contaminants, converting VOCs into CO<sub>2</sub> and H<sub>2</sub>O.

The photocatalytic conversion of air pollutants consists of the mineralization of the contaminants in a photoreactor using a semiconductor catalyst under an irradiation source. The photons are absorbed on the semiconductor surface forming electron (e<sup>-</sup>) and hole (h<sup>+</sup>) pairs. These electron and hole pairs can either recombine with each other (decreasing the efficiency of the photocatalytic

process) or react alternatively with oxygen and water adsorbed on the photocatalyst surface forming •OH radicals, superoxide anions and hydrogen peroxide. The formed •OH can further react with adsorbed organic molecules converting them into CO<sub>2</sub> and water. [6].

Studies in photocatalysis in air have mostly focused on semiconductor synthesis and best operating conditions. However, while larger scale photoreactors in the 10–100 L volume range were studied [7–10], efficiency evaluations were not performed rigorously.

Thus, to progress in this area, one has to establish both efficient semiconductor immobilization and extent of photon utilization. Photon use can be demonstrated with suitable Quantum Yield (QY) [11]. For instance, the frequently considered QY, based on photoconverted molecules to incident photons, does not provide a phenomenologically based performance assessment [12–15]. A modified and more suitable QY can be considered using the ratio of the •OH radicals consumed over the photons absorbed [16]. The evaluation of absorbed photons is of high relevance for adequate reaction modeling and photoreactor design [17]. This task which is at times challenging, is seldom adopted by researchers with a few exceptions [18,19].

To address these issues, the present study reports a detailed Quantum Efficiency analysis of a TiO<sub>2</sub> coated mesh in a 55.1 L scaled-up Photo-CREC-Air Reactor. Two techniques are considered:

\* Corresponding author.

E-mail address: [hdelasa@eng.uwo.ca](mailto:hdelasa@eng.uwo.ca) (H. de Lasa).

## Nomenclature

$A_{irr}$	Irradiated mesh area holding the catalyst, cm <sup>2</sup>
$A_c$	Coated mesh area, cm <sup>2</sup>
$E_{av}$	Average energy of a photon at a wavelength range, J/mol photon
$K^A_{Acetone}$	Acetone adsorption constant, l/ $\mu$ mole
$C_{Acetone,g}$	Concentration of acetone in the gas phase, $\mu$ mole/l
$L_{opt}$	Optimum TiO <sub>2</sub> coating thickness, cm
$P$	Rate of photons (photon/s)
$P_{el}$	Rate of photons reaching the surface of the TiO <sub>2</sub> coated mesh (photon/s)
$P_R$	Rate of photons reflected by the TiO <sub>2</sub> coated mesh (photon/s)
$P_t$	Rate of photons passing through the TiO <sub>2</sub> coated mesh (photon/s)
$q(\theta, z, \lambda, t)$	Irradiation measured by the spectrometer (W/cm <sup>2</sup> ·nm)
$q_a$	Absorbed irradiation in the TiO <sub>2</sub> immobilized mesh (W/cm <sup>2</sup> ·nm)
$Q_{acetone}$	Amount of acetone adsorbed on the solid, $\mu$ mole/g <sub>cat</sub>
$Q_{acetone,max}$	Maximum amount of acetone adsorbed on the solid, $\mu$ mole/g <sub>cat</sub>
$QY$	Quantum yield based on $\bullet$ OH radical consumption
$\eta_w$	Quantum yield per photocatalyst weight, 1/g
$QY_{max}$	Maximum based quantum yield
$\eta_{w,optimum}$	Optimum quantum yield per photocatalyst weight, 1/g
$r$	Radiation measurement radius (cm)
$r_{Acetone,g}$	Reaction rate of acetone in the gas phase, $\mu$ mole/m <sup>2</sup> ·min
$r_{Acetone,T}$	Total reaction rate of acetone, $\mu$ mole/m <sup>2</sup> ·min
$r_{CO_2}$	Total reaction rate for the production of CO <sub>2</sub> , $\mu$ mole/m <sup>2</sup> ·min
$r_{\bullet OH}$	Total reaction rate of formation of OH radical groups per unit weight of irradiated catalyst, $\mu$ mole/m <sup>2</sup> ·min
$r_{\bullet OH,j}$	Reaction rate of OH radicals in reaction step $j$ , $\mu$ mole/m <sup>2</sup> ·min
$r_{i,j}$	Reaction rate of component $i$ in reaction step $j$ , $\mu$ mole/m <sup>2</sup> ·min
$r_{i,T}$	Total reaction rate of the photoconversion of model pollutants, $\mu$ mole/m <sup>2</sup> ·min
$V$	Total system volume, l
$z$	Axial coordinate (cm)
$W$	Photocatalyst weight (g <sub>cat</sub> )

## Acronyms

AAS-ACM	Air assisted spray—automatized coating method
CREC	Chemical reaction engineering centre
EDX	Energy dispersive X-ray spectroscopy
QY	Quantum yield
SC	Spread coating method
SEM	Scanning electron microscope
UV	Ultra violet
VOC	Volatile organic compound

## Subscripts

<i>ads</i>	Adsorbed
<i>av</i>	Average
<i>irr</i>	Irradiated
<i>max</i>	Maximum

<i>min</i>	Minimum
<i>opt</i>	Optimum

## Greek letters

$\alpha$	Fraction of acetone following the partial oxidation step to acetaldehyde
$\varepsilon$	TiO <sub>2</sub> coating porosity
$\rho_{TiO_2}$	Mass density of TiO <sub>2</sub> , g/cm <sup>3</sup>
$\nu_{\bullet OH}$	Stoichiometric coefficient for the consumption of the OH radical
$\nu_{Acetone}$	Stoichiometric coefficient of acetone in the conversion of acetone to acetaldehyde
$\nu_{CO_2,a}$	Stoichiometric coefficient of CO <sub>2</sub> in the conversion of acetone to acetaldehyde
$\nu_{\bullet OH,j}$	Stoichiometric coefficient of the OH radical in reaction step $j$
$\nu_{H_2O,j}$	Stoichiometric coefficient of H <sub>2</sub> O in reaction step $j$
$\nu_{h,j}$	Stoichiometric coefficient of component $h$ in reaction step $j$
$\nu_{i,j}$	Stoichiometric coefficient of component $i$ in reaction step $j$
$\theta$	Tangential coordinate
$\lambda$	Radiation wavelength, nm
$\lambda_{max}$	Upper bound of wavelength in the range of interest, nm
$\lambda_{min}$	Lower bound of wavelength in the range of interest, nm

Spread Coating (SCM) and Air Assisted Spray (AAS) in conjunction with an Automatized Spinning Coating (TiO<sub>2</sub>-AAS-ASC). Homogeneity, reliability and particle agglomeration are evaluated for both procedures. Macroscopic radiation balances allow one to establish the rate of absorbed photons. In addition, experimental runs using acetone photodegradation experiments lead to calculations of hydroxyl radical consumption rates. The calculation of these hydroxyl radical rates includes (a) the series-parallel mechanism of acetone degradation to acetaldehyde and CO<sub>2</sub> and (b) the adsorption of the species using Langmuir parameters. All this leads to a rigorous QY calculation method, for the immobilized TiO<sub>2</sub> photocatalysts.

## 2. TiO<sub>2</sub> immobilization in photoreactors

A significant body of technical literature has already been focused on the synthesis of semiconductors with higher photoactivity and lower band gaps for the photodegradation of pollutants in air [1,2]. The application of these nanomaterials in relevant process scales requires the TiO<sub>2</sub> deposition on a substrate. The coated material should also have the adequate photoactivity, homogeneity and stability.

In this respect, both the support and immobilization of TiO<sub>2</sub> play an important role in the photocatalyst performance. A reliable technique for TiO<sub>2</sub> immobilization has to be established to provide the following:

- Strong adherence between the TiO<sub>2</sub> and the support.
- Unmodified TiO<sub>2</sub> crystal structure during preparation and immobilization.
- Uniform coating of different support surfaces and geometries.
- High degree of TiO<sub>2</sub> layer irradiation.

A number of methods for TiO<sub>2</sub> coatings on different support materials for the photodegradation of pollutants are reported in the

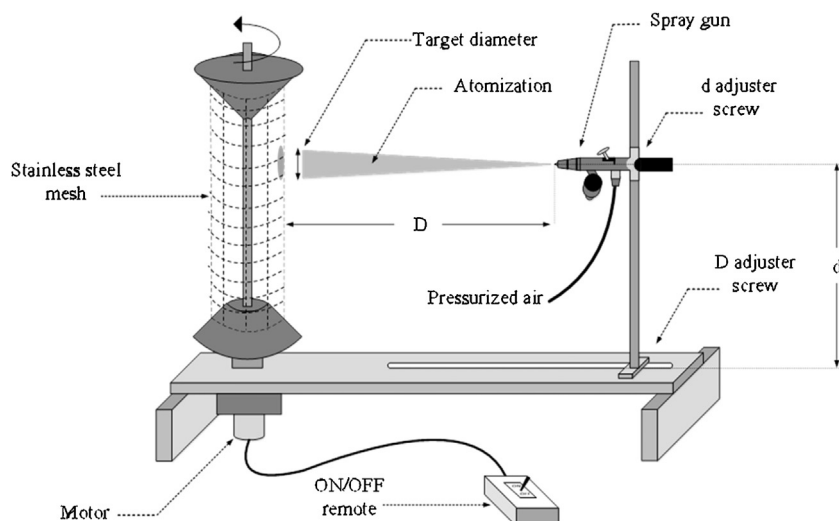


**Fig. 1.** Schematic Diagram of the Automatized Spray Coating (ASC) System. In the ASC apparatus, the spray gun can be moved both vertically and horizontally. The step size for vertical movement of the spray gun is 2 cm. This is the expected size of the target diameter.

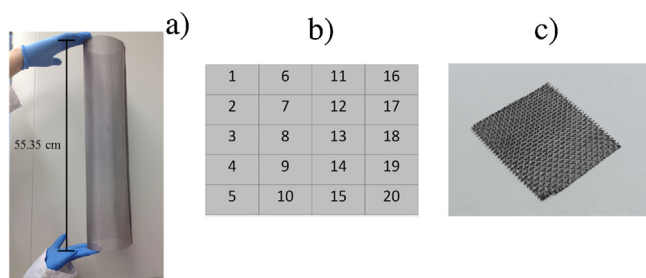


**Fig. 2.** (a) Photo of the Entire 55.4 cm × 34.7 cm TiO<sub>2</sub> Coated Stainless Steel Mesh. (b) Schematic Representation of the 20 Identified Area Sections of the TiO<sub>2</sub> Impregnated Mesh Sample. (c) Photo of the 1 in<sup>2</sup> Impregnated Mesh Considered for Further Analyses.

literature [20]. This includes physical and chemical vapor deposition, anodic oxidation, atomic layer coating, magnetron sputtering, pulsed laser coating, electro deposition, dip coating [21–29]. Dip coating is in fact, one of the most popular methods. It does not require hazardous chemicals or high energy consumption.

However, dip coating appears to present issues with large surfaces and geometries. For instance, in the case of TiO<sub>2</sub> deposited on a mesh, the impregnating solution may block the mesh openings. Pressurized air may be required then to eliminate the excess of solution [21]. This additional step can affect the homogeneity of the TiO<sub>2</sub> deposited. Spread coating is also a popular technique due to its low cost and simplicity. It can be applied without damaging the catalyst structure [10,30]. Spread coating was implemented in the past by our group for the TiO<sub>2</sub> immobilization with the aim of degrading VOCs. This consists of brush spreading sonicated TiO<sub>2</sub> slurry on a mesh followed by drying or calcination. Degussa P25 coated on a mesh using this method showed high photocatalytic degradation of toluene [31], acetone [32,33], isopropanol [34] and acetaldehyde [35]. Despite the advantages of this technique, the search for an improved method is needed. This is required to provide a better control of the titanium dioxide homogeneity, loading, stability under flow and a better degree of semiconductor utilization.

The spray technology is a well-known technique. It includes all the advantages of dip and spread spray coating. It has been widely used in nanoparticle synthesis [36–38]. Spray coating in particular, is very convenient for all types of geometries (including metallic meshes). It is easy to scale up. It can be applied in combination

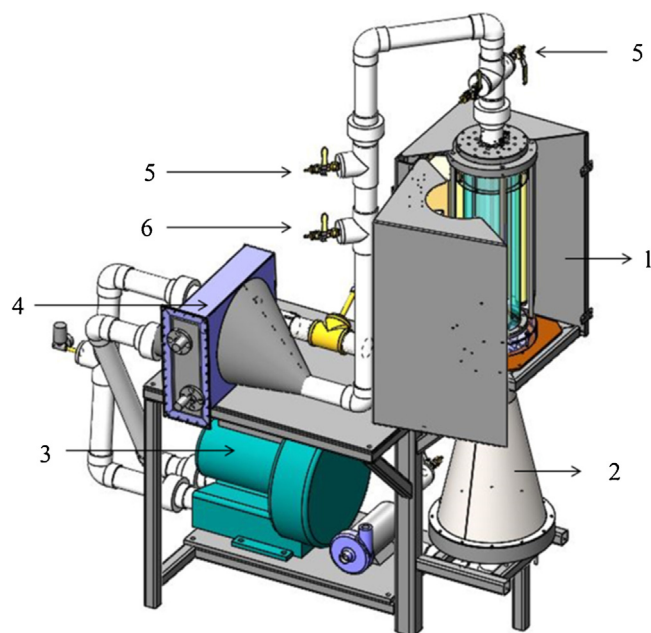


**Fig. 3.** Schematic Diagram of the Photo-CREC Degradation System: (1) reaction section, (2) venturi section, (3) blower, (4) cooler, (5) automatic sampling ports and (6) injection port.

with sol-gel [39–42], pyrolysis [43], electrostatic technique [39] or spray drying [8,44,45]. Spray coating should in principle lead to a high dispersion of TiO<sub>2</sub> particles with high photoactivity [8]. However, and in spite of this progress, we believe that coated mesh characterizations are required for further progress in the design of scaled-up photocatalytic reactor units.

In this work, we developed a TiO<sub>2</sub>-AAS-ASC coating method. It is proven that this approach leads to a uniform and stable coating with little particle agglomeration and high QYs.

### 3. Experimental methods

#### 3.1. Mesh preparation

The TiO<sub>2</sub> was immobilized on a stainless steel 304 woven wire mesh supplied by Ferrier Wire (40 × 40 mesh count, 36% open area,

0.01 in wire diameter). With this aim, two methods were used: (a) spread coating (TiO<sub>2</sub>-SC) and (b) air assisted spray with automatized spinning (TiO<sub>2</sub>-AAS-ASC). The selection of this mesh was carefully effected to balance the open areas and the wire covered areas. With this end, a mesh with a 64% irradiated area and a 36% open area was selected. This approach provided: (a) minimum opening blockages with TiO<sub>2</sub> particles following impregnation, (b) a high air flow in the mesh openings with a limited pressure drop, (c) a high degree of irradiation of the mesh surface.

The TiO<sub>2</sub>-SC method involved the following steps: (a) a water slurry containing 8 wt% nonporous 35–36 m<sup>2</sup>/g Aeroxide TiO<sub>2</sub> P25 was prepared; (b) The particle slurry was applied with a brush on the stainless steel mesh. Following a time of approximately 10 min, the mesh was blown with compressed air to eliminate the excess of solution clogging the wire openings. The coated mesh was dried at room temperature for 24 h.

Concerning the TiO<sub>2</sub>-AAS-ASC, the preparation procedures can be summarized as follows: (a) A 150 Badger nozzle gun was positioned at 30 cm from the stainless steel mesh surface (30 cm), (b) The drum holding the stainless steel mesh was rotated at 12 RPM, (c) The air pressure and TiO<sub>2</sub> concentration were set at 20 psia and 16 wt%, respectively. The flow the TiO<sub>2</sub> slurry spray was set at 15.7 mL/min. Fig. 1 reports a schematic description of the AAS-ASC system.

It was observed that changes of the rotating speed, distance of the nozzle to the target, air pressure and TiO<sub>2</sub> concentration were all factors influencing TiO<sub>2</sub> loadings and TiO<sub>2</sub> agglomeration. Furthermore, finally selected AAS-ASC coating conditions were chosen based on the best TiO<sub>2</sub> slurry flow leading to desirable droplet impact force, controlled droplet sizes and TiO<sub>2</sub> homogeneity. It was observed that a 16 wt% TiO<sub>2</sub> slurry with an atomized slurry of 1.31 mL per drum revolution were the best.

On this basis, the expected TiO<sub>2</sub> mass sprayed on the mesh is 5.8 gr. The actual amount of TiO<sub>2</sub> deposited on the mesh as established via gravimetry, was however, 2.2 gr on a 1220 cm<sup>2</sup> stainless steel wire mesh surface. This shows that the AAS-ASC displays an impregnation efficiency of 38%, with the resulting coating being both homogenous and free of agglomerates.

On the basis of the above, different TiO<sub>2</sub> loadings implemented in order to assess acetone photodegradation activity were as follows: 1 wt% to 3 wt% TiO<sub>2</sub> for TiO<sub>2</sub>-SC and 0.8 wt% to 2 wt% for TiO<sub>2</sub>-AAS-ASC.

### 3.2. Mesh characterization

The TiO<sub>2</sub> loading homogeneity was characterized by a local gravimetric method for both the TiO<sub>2</sub>-SC and TiO<sub>2</sub>-AAS-ASC (Fig. 2). This encompassed the following steps: (a) a TiO<sub>2</sub> immobilized mesh was divided into segments of 1 in<sup>2</sup> square area; (b) the TiO<sub>2</sub> was removed from each segment using an ultrasonic bath for 2–3 h; (c) the local loading was calculated using a weight difference. Furthermore, the morphology and the thickness of the TiO<sub>2</sub> film were characterized by a Hitachi S-4500 Field Emission Scanning Electron Microscope (SEM) with a Quartz PCI XOne SSD X-Ray Analyzer. Finally, the elemental analysis on the TiO<sub>2</sub> coated mesh was performed with Energy-Dispersive X-Ray Spectroscopy (EDX).

### 3.3. Photocatalytic reactor setup

The Photo-CREC-Air Reactor is a 55.1 L total volume unit operated in the CREC laboratories [32]. This unit was employed in the present study for the photodegradation of air pollutants. The present configuration is the result of significant design improvements as established using Computational Fluid Dynamics (CFD) [31,46]. The Photo-CREC-Air Reactor design provides an effective interaction between a gas stream and the irradiated TiO<sub>2</sub> immobi-

lized on the mesh. In addition, the modified Photo-CREC-Air Reactor permits macroscopic energy balances allowing the measurements of incident, transmitted and reflected radiation.

The entire Photo-CREC-Air can be viewed as a closed loop system. Fig. 3 reports the main sections of the Photo-CREC-Air Reactor. In this unit, air is recirculated through the reactor with the help of a GASP gas blower. Air is pumped into a stainless steel Venturi, and subsequently driven into the reaction section. Before the air is sent back to the blower, it is cooled down using water at 5–10 °C. This allows the reactor operation at close to isothermal conditions (≈44 °C). The reaction section includes eight 15 W nominal power UV lamps (EiKO Global, LLC) surrounding a quartz glass cylindrical tube (Fig. 4a). The radiation wavelength supplied by the UV lamps ranges from 325 to 380 nm. The UV source irradiates a total coated mesh area of 1042 cm<sup>2</sup>. The TiO<sub>2</sub> coated mesh is located inside a quartz glass tube, supported by a bullet nose bottom. This design allows an even lengthwise gas cross-flow from the annular region to the interior of the mesh (Fig. 4b).

### 3.4. Irradiation measurements

The radiation in the Photo-CREC-Air Reactor is measured by an optical probe as described in Fig. 3. This optical probe is inserted through a perforated plate located on top of the Photo-CREC-Air Reactor. Measurements can be made using this probe along the axial length (z) at various circumferential reactor positions (θ). The optical probe itself is constituted of a short 1 cm horizontal entry section, a specular surface oriented at 45° and a 2 m vertical fiber optic connected to a Stellarnet EPP3000 Spectrometer. This spectrometer measures radiation in the 200–1100 nm wavelength range. The combined fiber optic probe-spectrometer system allows one to establish the distribution of irradiation in the Photo-CREC-Air Reactor and as a result to perform a macroscopic radiation balance including:

- Radiation reaching the surface of the TiO<sub>2</sub> coated mesh ( $P_{el}$ ) (Fig. 5b-1).
- Radiation transmitted through the TiO<sub>2</sub> coated mesh ( $P_t$ ) (Fig. 5b-2).
- Radiation reflected by the TiO<sub>2</sub> coated mesh ( $P_R$ ) (Fig. 5b-3).

Regarding the incident, reflected and transmitted photon rates ( $P_{el}$ ,  $P_t$  and  $P_R$ ), they were calculated using the following eq. involving  $z$ ,  $\theta$  and  $\lambda$  coordinates,

$$P = \frac{\int_{\lambda_{\min}}^{\lambda_{\max}} \int_0^{\infty} \int_0^{2\pi} q(\theta, z, \lambda) r d\theta dz d\lambda}{E_{av}} \quad (1)$$

where  $q(\theta, z, \lambda)$  represents the radiation measured in W/cm<sup>2</sup>-nm;  $\lambda$  stands for the radiation wavelength;  $\theta$  and  $r$  represent the angular and radial positions and  $E_{av}$  denotes the average photon energy.

On the basis of these measurements, local macroscopic radiation balances were calculated using the following:

$$P_a = P_{el} - P_t - P_R \quad (2)$$

where  $P_a$  represents the photons absorbed by the immobilized photocatalyst.

### 3.5. Acetone photocatalytic degradation

The performance of the Photo-CREC-Air Unit with both TiO<sub>2</sub>-SC and TiO<sub>2</sub>-AAS-ASC meshes was established in the present study, utilizing the photocatalytic degradation of acetone. Different initial concentrations were considered: 25, 37 and 50 μmol/L. In



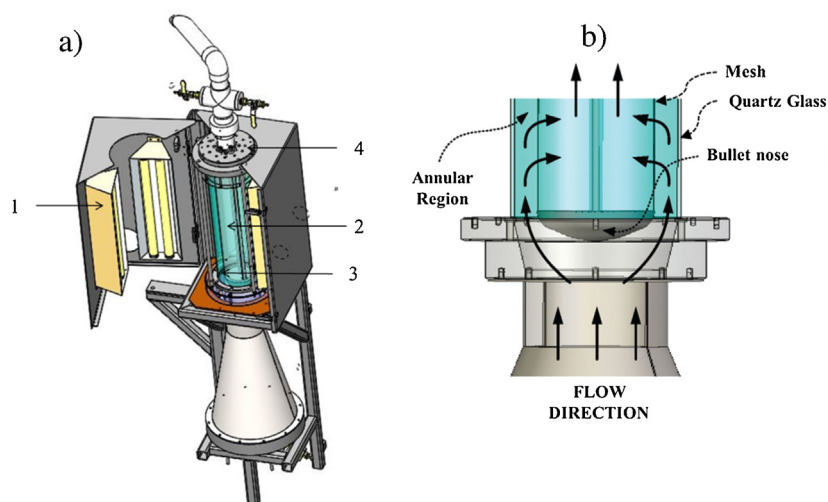


**Fig. 4.** (a) Schematic Diagram of the Reaction Section: (1) surrounding UV lamps, (2) coated stainless steel mesh, (3) quartz glass and (4) perforated plate. (b) schematic Diagram of the Cross-Flow Air Circulation through the  $\text{TiO}_2$  Coated Mesh in the Photo-CREC-Air Reactor.

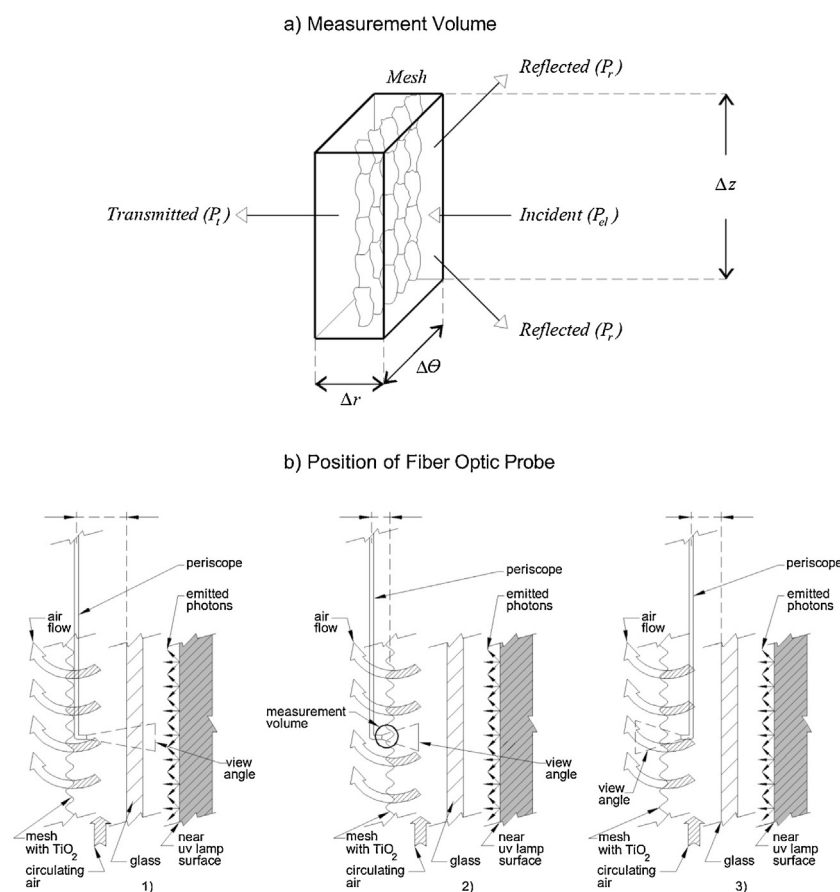


**Fig. 5.** (a) Schematic Diagram of the Selected Control Volume for Macroscopic Local Radiation Balances. (b) Schematic Diagram of the Optical Probe Location in the Photo-CREC-Air Reactor for Radiation Measurements as: (1) *Incident radiation* ( $P_{el}$ ): the optical probe is placed in between the coated mesh and the quartz glass facing the UV-lamps, (2) *Transmitted Radiation* ( $P_t$ ): the optical probe is placed behind the coated mesh, (3) *Reflected Radiation* ( $P_r$ ): the optical probe placed in between the mesh and the quartz glass facing the coated mesh.

terms of analytical equipment, a Shimadzu 2014 Gas Chromatograph followed by a methanizer and a flame ionization detector (FID) were used to monitor  $\text{CO}_2$ , acetone and intermediate species. These chemical species were separated using a Porapak Q column. Retention times for  $\text{CO}_2$ , acetone and acetaldehyde were 2.2, 8.2 and 5 min, respectively using a  $55^\circ\text{C}/\text{min}$  temperature ramp until

$185^\circ\text{C}$  was reached. Once this thermal level was achieved, the GC furnace was kept at this temperature for 8 min.

Photodegradation experimental runs were performed using the following steps: (a) a 0.100–1 mL of acetone was injected into the Photo-CREC-Air Unit via the liquid injection port. (b) The injected liquid samples vaporized instantaneously and were allowed to mix

**Table 1**  
EDX Analysis of Different Area Sections of the TiO<sub>2</sub> Coated Stainless Steel Meshes Using TiO<sub>2</sub>-SC and TiO<sub>2</sub>-AAS-ASC Methods.

		C	O	Ti	Cr	Fe
TiO <sub>2</sub> -SC	Area 1	3.5	56.6	39.3		0.6
	Area 2	8.2	15.8	8.9	12.9	48.8
	Area 3	3.1	55.7	41.1		
TiO <sub>2</sub> -AAS-ASC	Area 1	2.4	36.3	59.9	0.3	1.2
	Area 2	3.5	43.8	48.1	1.0	3.6
	Area 3	4.5	51.9	41.9	0.3	1.2

for 30 min. This time period, designated as the dark period is the required time to allow all processes including adsorption to reach equilibrium. (c) Following this, the UV lamps were turned on. Irradiation was typically on for about 60–150 min. Gas samples were taken every 18 min, using an automatized sampler connected to the gas chromatograph. (d) Once all organic species were depleted and CO<sub>2</sub> levels were established, runs were considered to be completed. In between runs, the impregnated TiO<sub>2</sub> was regenerated and cleaned by flushing air free of organic species, under UV irradiation during 10 min. The compositions of the various chemical species at different irradiation times were recorded for further data analysis and kinetic modeling.

### 3.6. Adsorption isotherm

Regarding the organic species adsorbed on the TiO<sub>2</sub> coated mesh at equilibrium, the Langmuir equation provides a good description [32]. On this basis, adsorption isotherms were developed for both TiO<sub>2</sub>-SC and TiO<sub>2</sub>-AAS-ASC meshes. The experimental procedure was as follows: (a) a set 0.1–1 mL of acetone volume was injected into the Photo-CREC-Air Reactor with the near UV lamps turned “off”. (b) Air samples were taken periodically (every 18 min) until the gas phase acetone concentration reached a stable level. This condition was considered adsorption at equilibrium. (c) This procedure was repeated several times at various initial acetone concentrations in the 13–50 μmol/L range.

## 4. Results and discussion

### 4.1. Mesh characterization

Mesh characterization is of critical importance to determine both for TiO<sub>2</sub> dispersion and mesh coating quality. With this end, a gravimetric method and SEM-EDX were employed for characterization of both TiO<sub>2</sub>-SC and TiO<sub>2</sub>-AAS-ASC. Fig. 6 reports the local TiO<sub>2</sub> loading distribution for a 2.2 wt%: (a) TiO<sub>2</sub>-SC mesh loading and (b) TiO<sub>2</sub>-AAS-ASC mesh loading. One can notice that the local loadings of TiO<sub>2</sub>-SC (Fig. 6a) display a standard deviation of 0.62 wt%. In contrast, one should observe that the TiO<sub>2</sub>-AAS-ASC (Fig. 6b) shows a much reduced 0.12 wt% standard deviation. This demonstrates the more uniform coating achieved with the TiO<sub>2</sub>-AAS-ASC mesh versus the TiO<sub>2</sub>-SC.

Table 1 shows Energy Dispersive X-Ray Spectroscopy (EDX) analysis for randomly selected areas on the TiO<sub>2</sub>-SC and TiO<sub>2</sub>-AAS-ASC meshes. The data of this table further supports the findings that better coatings are obtained with the TiO<sub>2</sub>-AAS-ASC mesh rather than with the TiO<sub>2</sub>-SC mesh.

One can also see in Table 1, that if the Ti element is used as the tracing element for TiO<sub>2</sub>, then the 1–3 areas, yielding Ti on the TiO<sub>2</sub>-SC mesh, vary in the 8.9–41.1% wide range. On the other hand, when using the TiO<sub>2</sub>-AAS-ASC mesh, the Ti element as measured by SEM-EDX was observed to be changing both in a higher and narrower 40–60% range. The observed Cr, C and Fe elements can be used to trace cracks in the TiO<sub>2</sub> films. For instance, in the case of TiO<sub>2</sub>-SC,

high Fe, Cr and C variations (0.6–48% Fe, 0–12% Cr and 3.1–8.2% C) show significant film thickness changes. On the other hand, close to constant values for TiO<sub>2</sub>-AAS-ASC (1.2–3.6% Fe, 0.3–1% Cr, 2.4–4.5% C) demonstrate a rather uniform film thickness. In other words, SEM-EDX can be used to confirm the better properties of the TiO<sub>2</sub>-AAS-ASC mesh coating.

In order to further support the results of the TiO<sub>2</sub>-AAS-ASC better-quality coating, SEM micrographs were taken from both 3 wt% TiO<sub>2</sub>-SC and 1 wt% TiO<sub>2</sub>-AAS-ASC samples.

Figs. 7a and b report the SEM micrographs for the TiO<sub>2</sub>-SC and the TiO<sub>2</sub>-AAS-ASC impregnated meshes, respectively. One can notice that in Fig. 7a, the TiO<sub>2</sub>-SC coating presents light gray areas showing uncoated stainless steel (island on the mesh) and areas in dark gray showing the TiO<sub>2</sub> coating. In this case, one can also observe that TiO<sub>2</sub> accumulates mainly in the wire joints leaving uncovered islands in other mesh surfaces. Thus, the TiO<sub>2</sub>-SC mesh leads to distinctive coated and uncoated regions. On the other hand, for TiO<sub>2</sub>-AAS-ASC, Fig. 7b shows an essentially fully coated mesh surface with a uniform TiO<sub>2</sub> layer over the entire surface. This is a mesh surface free of shiny uncovered areas. In spite of this, it was also noticed that increasing the TiO<sub>2</sub> loading led to films more prone to the formation of cracks.

Fig. 8 reports SEM micrographs showing the TiO<sub>2</sub>-SC and TiO<sub>2</sub>-AAS-ASC coating thicknesses. Fig. 8a gives a TiO<sub>2</sub>-SC thickness of 22.9 μm while Fig. 8b provides a TiO<sub>2</sub>-AAS-ASC thickness in the 6–10 μm range. These results provide evidence of the much thinner thickness provided by the TiO<sub>2</sub>-AAS-ASC.

Fig. 9 shows an overview of the TiO<sub>2</sub> particles on the TiO<sub>2</sub>-SC and TiO<sub>2</sub>-AAS-ASC impregnated mesh areas. One can notice that the agglomeration of particles when using the TiO<sub>2</sub>-SC is clearly more predominant than that when utilizing the TiO<sub>2</sub>-AAS-ASC. In addition, in the case of the TiO<sub>2</sub>-AAS-ASC, the particles are more homogeneously distributed on the surface than when using the TiO<sub>2</sub>-SC.

On this basis, one can attest that the differences of the particle homogeneous distribution and particle agglomeration are coating method dependant. The changes of slurry flow, motor speed and air pressure are all factors leading to a controlled deposition of the TiO<sub>2</sub> coating. In fact, the small droplets produced by the atomizer lead to a better dispersion of the TiO<sub>2</sub> particles generating as a result less agglomeration [8].

Furthermore, and in order to establish the stability of the prepared TiO<sub>2</sub>-AAS-ASC coated mesh, a 1906 cm<sup>2</sup> mesh area, was exposed to 375 m<sup>3</sup>/h of air flow during 1000 h. In this case, it was observed that when using the gravimetric method, less than 10 wt% of the TiO<sub>2</sub> loaded was lost (see Appendix B). Therefore, one can conclude that the TiO<sub>2</sub> particle adhesion forces to the stainless steel mesh in the TiO<sub>2</sub>-AAS-ASC are significant and are in excess to the forces promoted by the fluid flow in the Photo-CREC-Air unit.

### 4.2. Photocatalytic activity: effect of the TiO<sub>2</sub> loading and of the initial acetone concentration

The prepared TiO<sub>2</sub>-SC and TiO<sub>2</sub>-AAS-ASC meshes were evaluated in terms of photocatalytic activity for the degradation of acetone in the Photo-CREC-Air Reactor. Fig. 10 reports the effect of the semiconductor loading on the initial reaction rate. An initial acetone concentration of 25 μmol/L was considered for these experiments. The data reported in Fig. 10 was the result of 9 repeats developed per operating condition.

Fig. 10 reports an increase in the initial acetone conversion rate with the TiO<sub>2</sub> loading. This is the case for both TiO<sub>2</sub>-SC and TiO<sub>2</sub>-AAS-ASC. In this respect, one can observe that the initial photoconversion rate does not increase significantly once 2.5 wt% and 1 wt% were respectively reached for TiO<sub>2</sub>-SC and TiO<sub>2</sub>-AAS-ASC. Thus, one can conclude that the TiO<sub>2</sub>-AAS-ASC displays a level-

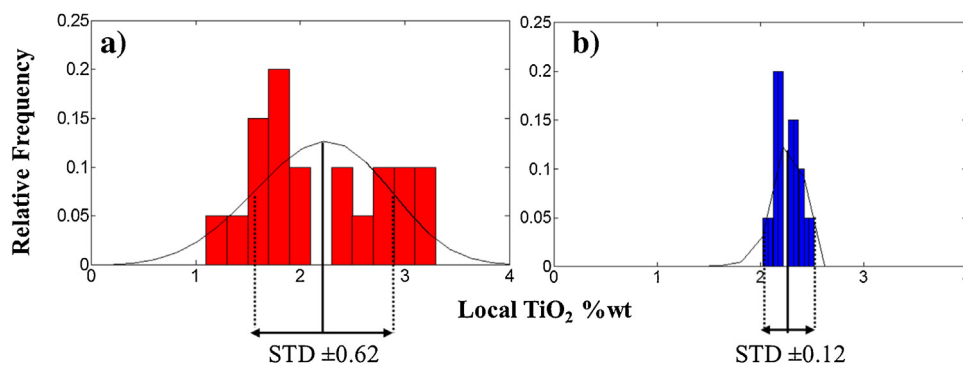


Fig. 6. TiO<sub>2</sub> Local Weight Loading Distribution on the Mesh Prepared using (a) the TiO<sub>2</sub>-SC method and (b) the TiO<sub>2</sub>-AAS-ASC method.

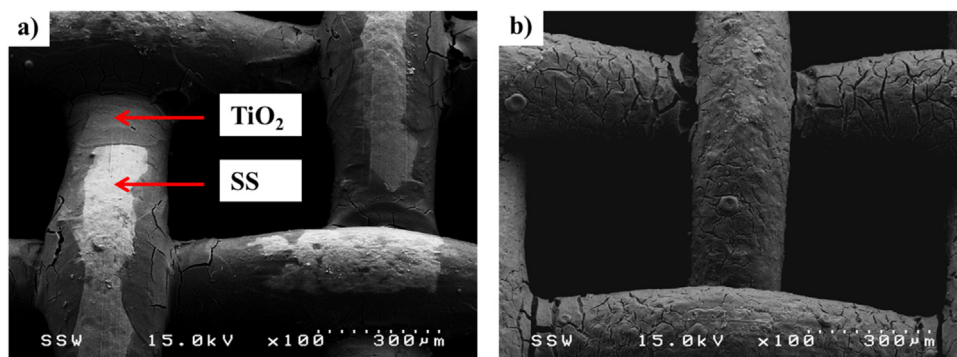


Fig. 7. SEM Micrographs of Stainless Steel Mesh Coated with (a) 3 wt% TiO<sub>2</sub> using the TiO<sub>2</sub>-SC and (b) 1% TiO<sub>2</sub> using the TiO<sub>2</sub>-AAS-ASC.

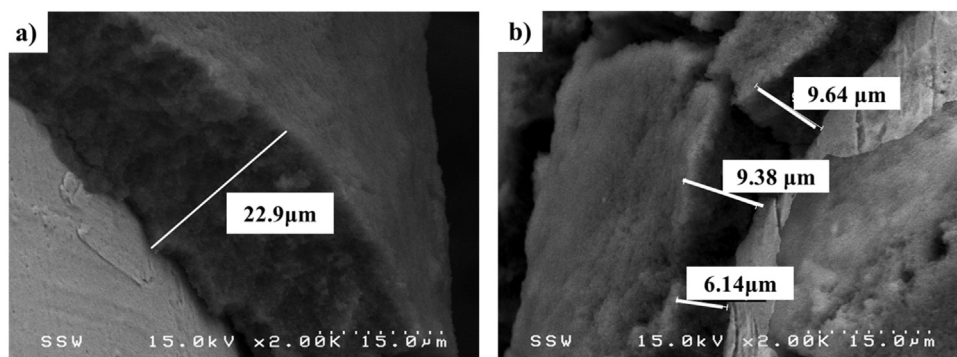


Fig. 8. SEM Micrographs of Measured TiO<sub>2</sub> Coating Thicknesses Using (a) TiO<sub>2</sub>-SC and (b) TiO<sub>2</sub>-AAS-ASC.

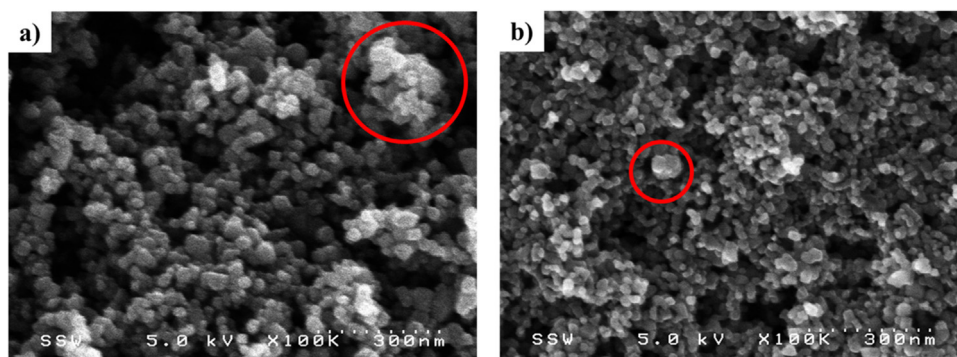
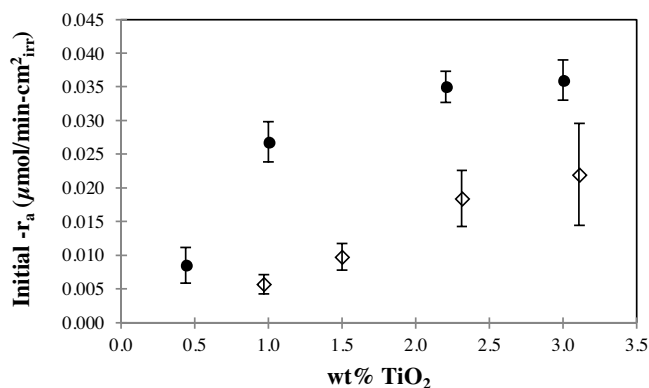


Fig. 9. SEM Micrographs of the Surface of the Impregnated TiO<sub>2</sub>: (a) TiO<sub>2</sub>-SC and (b) TiO<sub>2</sub>-AAS-ASC. Red circles show typical particle agglomerates. (For interpretation of the references to colour in this figure legend, the reader is referred to the web version of this article.).



**Fig. 10.** Effect of the  $\text{TiO}_2$  Loading on the Initial Reaction Rate per Mesh Irradiated Area when Using the  $\text{TiO}_2$ -SC (empty diamonds) and the  $\text{TiO}_2$ -AAS-ASC (solid circles). Reported data points and standard deviations included at least 4 repeats of independent experiments.

**Table 2**

Initial Acetone Photoconversion Rates per Unit Photocatalyst Weight in the Photo-CREC-Air Reactor using  $\text{TiO}_2$ -SC and  $\text{TiO}_2$ -AAS-ASC. Three initial acetone concentrations were considered: 25, 37 and 50  $\mu\text{mol}/\text{L}$ .

Acetone Initial Concentration ( $\mu\text{mol}/\text{L}$ )	Initial $r_{\text{acetone}}$ ( $\mu\text{mol}/\text{g}\cdot\text{min}$ )	
	$\text{TiO}_2$ -SC	$\text{TiO}_2$ -AAS-ASC
25	$4.3 \pm 12\%$	$13 \pm 17\%$
37	$5.4 \pm 12\%$	$16 \pm 12\%$
50	$5.9 \pm 8\%$	$18 \pm 22\%$

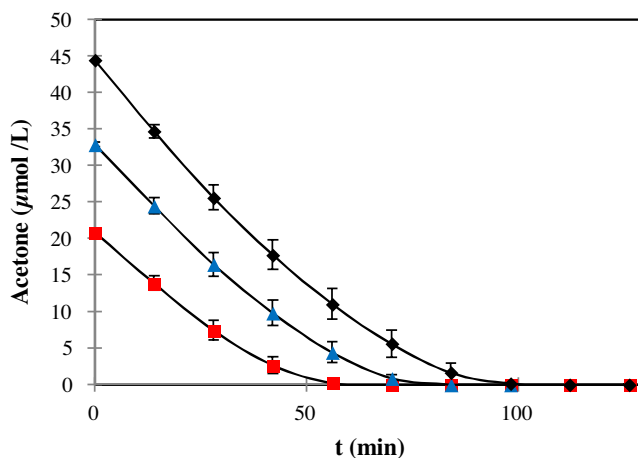
ing of the rate with 3 times less  $\text{TiO}_2$  than the one required for  $\text{TiO}_2$ -SC. Furthermore, the  $\text{TiO}_2$ -AAS-ASC appears to offer a more reliable alternative with initial photoconversion rates showing smaller standard deviations for repeats (5–10%). These standard deviations for the  $\text{TiO}_2$ -SC were in the 22% to 34% range.

Table 2 also reports the initial photoconversion rates for acetone. In this table, rates are based on the unit  $\text{TiO}_2$  weight. One can observe that the  $\text{TiO}_2$ -AAS-ASC yields a  $r_{\text{acetone}}$  close to 3 times that obtained with the  $\text{TiO}_2$ -SC. This is consistently true for all the runs developed using the  $\text{TiO}_2$ -AAS-ASC, and initial acetone concentrations in the 25–49  $\mu\text{mol}/\text{L}$  range.

Regarding the reported effects of the coated mesh on acetone photoconversion, one can attest that a higher photoactivity is achieved when using the  $\text{TiO}_2$ -AAS-ASC given: (a) its reduced particle agglomeration size in the coated layer, (b) its minimized particle agglomeration in the wire junctions. These favorable particle dispersions lead to better exposure of the  $\text{TiO}_2$  particles to incident photons.

These results are consistent with the data of Figs. 7–9, for the  $\text{TiO}_2$ -AAS-ASC. As stated, in this case, one can notice a more uniform and reproducible coating. The thickness of this coating reaches 6–10  $\mu\text{m}$ . This is considered to be the required thickness for complete photon absorption. In this respect, Peral and Ollis [47] reported a 99% near-UV light absorption within a  $\text{TiO}_2$  anatase layer of 4.5  $\mu\text{m}$ . Ibrahim and de Lasa [33] also showed a higher photocatalytic activity when the thickness of the layer of Degussa P25 on a fiberglass support reached 5.4  $\mu\text{m}$ . Jacoby et al. [48] also suggested that a 2  $\mu\text{m}$   $\text{TiO}_2$  thick layer participates in the photoreaction. Thus, it is concluded that the  $\text{TiO}_2$ -AAS-ASC of the present study provides a homogeneous and stable coating. This coating has a thickness close to the “optimum” one required for complete photon absorption and maximum photoconversion rates per unit  $\text{TiO}_2$  weight.

Figs. 11 and 12 report the acetone and  $\text{CO}_2$  concentrations formed at different initial conditions. The  $\text{TiO}_2$  coating used in all



**Fig. 11.** Changes of Acetone Concentration with Irradiation Time using the 1 wt%  $\text{TiO}_2$ -AAS-ASC Mesh. Three different initial concentrations were considered: (a) 25 ( $\square$ ), (b) 37 ( $\Delta$ ) and (c) 50  $\mu\text{mol}/\text{L}$  ( $\diamond$ ). Reported data points and standard deviations included at least 4 repeats of independent experiments.

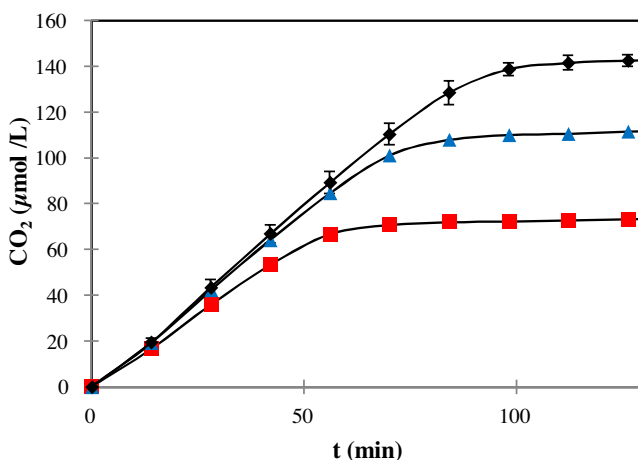


**Fig. 12.** Changes of  $\text{CO}_2$  Production for Acetone Photodegradation using the 1 wt%  $\text{TiO}_2$ -AAS-ASC Mesh. Three different initial acetone concentrations were considered: (a) 25 ( $\square$ ), (b) 37 ( $\Delta$ ) and (c) 50  $\mu\text{mol}/\text{L}$  ( $\diamond$ ). Reported data points and standard deviations included at least 4 repeats of independent experiments.

these cases was 1 wt%  $\text{TiO}_2$  for the  $\text{TiO}_2$ -AAS-ASC. One can notice a complete mineralization of the acetone after 56–100 min.

Furthermore, Figs. 13 and 14 display the acetone and  $\text{CO}_2$  concentration changes with irradiation time using a 3 wt%  $\text{TiO}_2$  on the  $\text{TiO}_2$ -SC. Once again, one can observe that the required irradiation times for complete mineralization using  $\text{TiO}_2$ -SC are in the 56–100 min range.

An important observation in Figs. 11–14, however, is that there is a higher variation in both acetone and  $\text{CO}_2$  measured concentrations when using the  $\text{TiO}_2$ -SC. This is particularly apparent for a 50  $\mu\text{mol}/\text{L}$  initial acetone concentration. These higher observed changes can be assigned to a less reproducible  $\text{TiO}_2$ -SC performance while compared to the  $\text{TiO}_2$ -AAS-ASC. One can notice that this is true in spite of the fact that the  $\text{TiO}_2$ -AAS-ASC requires 3 times less  $\text{TiO}_2$  than the  $\text{TiO}_2$ -SC.

#### 4.3. Adsorption isotherm

The Langmuir model is a good approach to describe the chemisorption at equilibrium [32]. This relates the adsorbed acetone species per unit  $\text{TiO}_2$  weight ( $Q_{\text{acetone}}$  in  $\mu\text{mole}/\text{g}$  of pho-



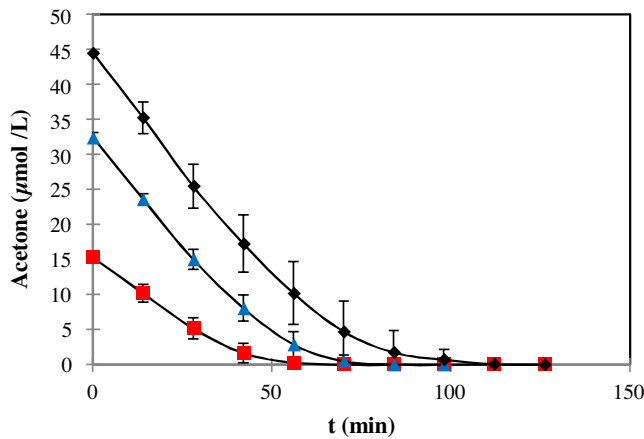


**Fig. 13.** Changes of Acetone Concentration with Irradiation Time using the 3% TiO<sub>2</sub> SC Mesh. Three different initial concentrations were considered: (a) 25 (□), (b) 37 (Δ) and (c) 50 μmol/L (◇). Reported data points and standard deviations included at least 4 repeats of independent experiments.

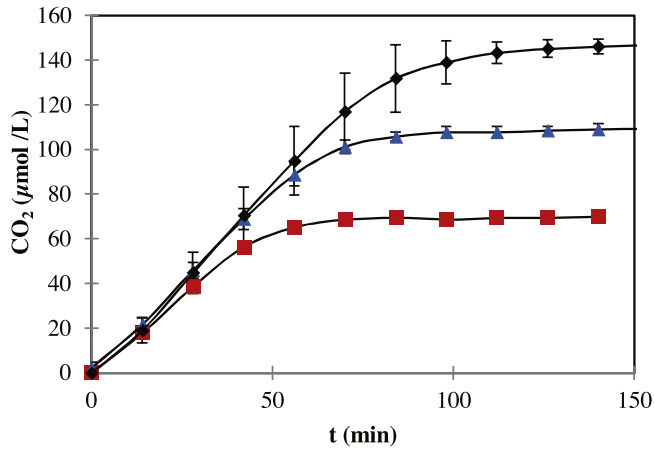


**Fig. 14.** Changes of CO<sub>2</sub> Production with Acetone Photodegradation using the 3 wt% TiO<sub>2</sub>-SC Mesh. Three different initial acetone concentrations were considered: (a) 25 (□), (b) 37 (Δ) and (c) 50 μmol/L (◇). Reported data points and standard deviations included at least 4 repeats of independent experiments.

**Table 3**  
Langmuir Parameters for the Adsorption Isotherm of Acetone on Immobilized Degussa P25 TiO<sub>2</sub>.

$Q_{\text{Acetone,max}}$ (μmol/g <sub>cat</sub> )	192	±38
$K^A_{\text{Acetone}}$ (l/μmol)	0.04	±0.012

tocatalyst) to the acetone concentration in the gas phase ( $C_{\text{Acetone,g}}$  in μmole/L) as follows:

$$Q_{\text{Acetone}} = Q_{\text{Acetone,max}} \frac{K^A_{\text{Acetone}} C_{\text{Acetone,g}}}{1 + K^A_{\text{Acetone}} C_{\text{Acetone,g}}} \quad (3)$$

where  $Q_{\text{Acetone,max}}$  (μmol/g<sub>cat</sub>) represents the acetone adsorbed as a monolayer per unit of TiO<sub>2</sub> weight; and  $K^A_{\text{Acetone}}$  (L/μmol) is the adsorption constant of acetone. The  $K^A_{\text{Acetone}}$  represents the affinity of the acetone to the immobilized TiO<sub>2</sub> surface.

Fig. 15 reports the adsorption isotherm for the TiO<sub>2</sub> coated meshes using both TiO<sub>2</sub>-SC and TiO<sub>2</sub>-AAS-ASC methods. This plot confirms the adequacy of the selected Langmuir model. One should note that the  $K^A_{\text{Acetone}}$  and  $Q_{\text{Acetone,max}}$  parameters as shown in Eq. (3) and reported in Table 3, were calculated using a nonlinear least squares regression algorithm. Although both films were deposited with different methods, the nature and structure of the TiO<sub>2</sub> remains the same. Thus, even if the time to reach the equilib-

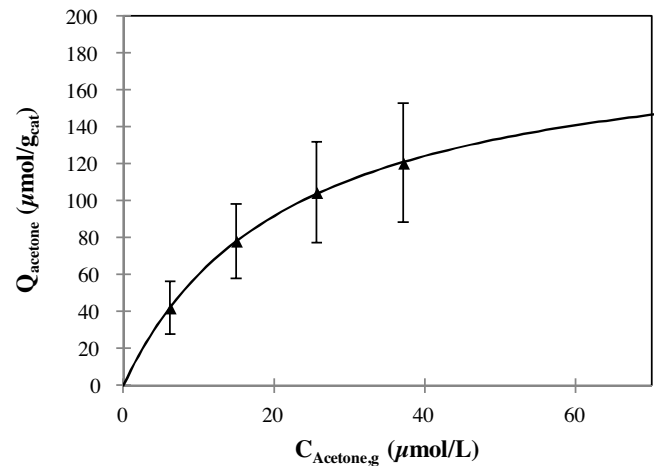


**Fig. 15.** Langmuir Adsorption Isotherm of Acetone on Degussa P25 TiO<sub>2</sub>. Both TiO<sub>2</sub>-SC and TiO<sub>2</sub>-AAS-ASC were considered to provide the adsorption at equilibrium isotherm. Reported data points and standard deviations included at least 10 repeats of independent experiments.

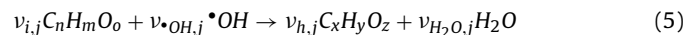
rium differs, the adsorption equilibrium parameters for both type of TiO<sub>2</sub> films are expected to be the same.

#### 4.4. Quantum yields

The Quantum Yield expresses photonic efficiencies in a photocatalytic reactor. A suitable definition for the QY is the ratio of •OH radicals consumed over the photons absorbed on the immobilized TiO<sub>2</sub> with a wavelength smaller than 388 nm [16], such as:

$$QY = \frac{\text{rate of } \bullet\text{OH consumed}}{\text{rate of photons absorbed by the photocatalyst with } \lambda \leq 388 \text{ nm}} \quad (4)$$

The rate of •OH radicals consumed as in Eq. (4), can be calculated using an “indirect method” based on the stoichiometric requirements for the oxidation of the observable chemical species [32]. Following this, the “i” lower oxidation state species ( $C_nH_mO_o$ ) can be converted with the help of •OH radicals to “h” higher oxidation state species ( $C_xH_yO_z$ ) as follows:



with  $\nu_{i,j}$  and  $\nu_{h,j}$  representing the stoichiometric coefficients for  $C_nH_mO_o$  and  $C_xH_yO_z$ , respectively. One should note that all species involved in the “j” step have to comply with carbon, hydrogen and oxygen element balances as shown in Eqs. (6a)–(6c):

$$\nu_{i,j} n - \nu_{h,j} x = 0 \text{ (Elemental carbon balance)} \quad (6a)$$

$$\nu_{i,j} m + \nu_{\bullet\text{OH},j} - \nu_{h,j} y - 2\nu_{H_2O,j} = 0 \text{ (Elemental hydrogen balance)} \quad (6b)$$

$$\nu_{i,j} o + \nu_{\bullet\text{OH},j} - \nu_{h,j} z - \nu_{H_2O,j} = 0 \text{ (Elemental oxygen balance)} \quad (6c)$$

Therefore,

$$r_{\bullet\text{OH},T} = \sum r_{\bullet\text{OH},j} = \sum \frac{\nu_{\bullet\text{OH},j}}{\nu_{i,j}} r_{i,j} \quad (7)$$

where  $r_{\bullet\text{OH},j}$  is the rate of •OH radical consumption in step “j” of the network,  $r_{i,j}$  is the reaction rate of the compound “i” in step “j”, and  $\nu_{i,j}$  is the stoichiometric coefficient for chemical species “i” in step “j”.

Using this approach, the total •OH consumption rate of Eq. (7), can be calculated as a summation of observable individual species rates times the ratio of corresponding stoichiometric coefficients.

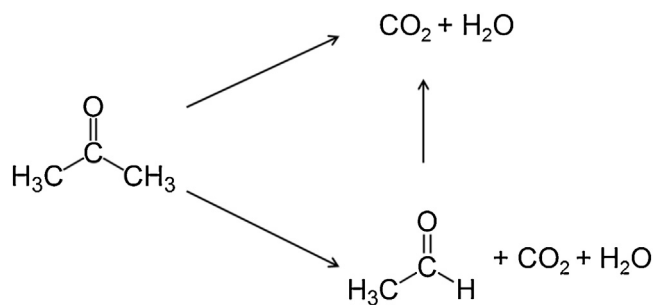


**Fig. 16.** Schematic Representation of the Proposed Mechanism for the Photodegradation of Acetone in the Photo-CREC-Air Reactor.

As a result, the QY as in Eq. (4) can be expressed as:

$$QY = \frac{-A_{irr} \sum_{j=1}^j r_{\bullet OH,j}}{P_a} = \frac{A_{irr} \sum_{j=1}^j \frac{\nu_{\bullet OH,j}}{\nu_{i,j}} r_{i,j}}{P_a} \quad (8)$$

where

$r_{\bullet OH,j}$  = the rate of  $\bullet OH$  radical consumption in step “j” (mole/cm<sup>2</sup><sub>irr</sub> s)

$r_{i,j}$  = the rate of “i” pollutant molecules degraded in the step “j” of the photoconversion (mole/cm<sup>2</sup><sub>irr</sub> s)

$\nu_{i,j}$  = the stoichiometric coefficient involved in the photoconversion of the species “i” in step “j”

$P_a$  = the rate of photons absorbed by the photocatalyst with  $\lambda \leq 388$  nm (mole of photons/s)

$A_{irr}$  = the total area of the irradiated photocatalyst-impregnated mesh, 1042 cm<sup>2</sup>

The Quantum Yield is calculated taken in account the considerations of Eq. (1). Thus, for a non-isoactinic reactor, the Eq. (8) becomes,

$$QY = \frac{A_{irr} \sum_{j=1}^j \frac{\nu_{\bullet OH,j}}{\nu_{i,j}} r_{i,j}}{\int_{\lambda_{min}}^{\lambda_{max}} \int_0^{2\pi} \int_0^{2\pi} q_a(\theta, z, \lambda) r d\theta dz d\lambda} \quad (8a)$$

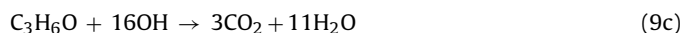
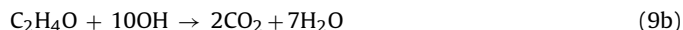
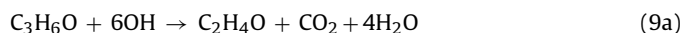
where  $q_a$  accounts for the absorbed radiation in  $\mu W/cm^2 \cdot nm$ . The denominator is calculated using macroscopic balances as described in Eq. (2). Integrals of the radiation in Eq. (8) were calculated with experimentally obtained data. A figure of the measured incident, transmitted and reflected radiation is reported in Appendix A.

#### 4.4.1. Reaction rates for $\bullet OH$ radicals

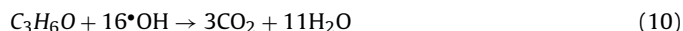
In order to establish the photoreaction rate for  $\bullet OH$  radicals, a reaction mechanism for acetone degradation has to be defined. In the present study, acetaldehyde was identified as an intermediate species in acetone photoconversion. This result is in agreement with other studies [49,50] which consider acetaldehyde as an intermediate species. This was shown using both Fourier Transform Infrared Spectroscopy and X-ray Photoelectron Spectroscopy.

In this respect, a series-parallel model, as shown in Fig. 16, appears to be suitable for the photodegradation of organic compounds on immobilized TiO<sub>2</sub> [12,51]. This reaction network is consistent with the expected local variations of photon density in the Photo-CREC-Air Unit.

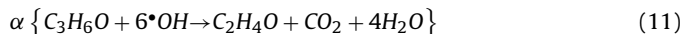
Furthermore, a  $\bullet OH$  radical consumption stoichiometry for every photodegradation step can be obtained considering the following:



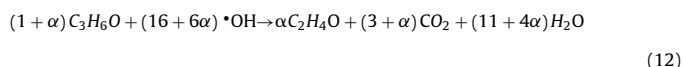
(a) The complete mineralization of acetone to CO<sub>2</sub>:



(b) The partial oxidation of acetone to acetaldehyde where  $\alpha$  is a factor that establishes the fraction of acetone involved in the partial oxidation step:



By multiplying Eq. (11) by an  $\alpha$  factor and by adding the resulting equation to equation 10, the following is obtained:



Thus, and on this basis, the  $\alpha$  and an  $\bullet OH$  consumption rate can be related as:

$$\frac{r_{Acetone,T}}{-(1 + \alpha)} = \frac{r_{CO_2}}{(3 + \alpha)}, \alpha = -\frac{(3r_{Acetone,T} + r_{CO_2})}{r_{Acetone,T} + r_{CO_2}} \quad (13)$$

$$r_{\bullet OH} = \frac{r_{CO_2} (16 + 6\alpha)}{(3 + \alpha)} \quad (14)$$

where  $r_{(CO_2)}$ , represents the rate of CO<sub>2</sub> formation,  $r_{Acetone,T}$  stands for the total rate of acetone conversion and  $r_{\bullet OH}$  denotes the  $\bullet OH$  radicals consumed in the degradation of acetone. All of these variables are expressed in  $\mu mole/m^2_{irr} \cdot min$ .

The  $r_{(CO_2)}$  rate can be calculated using the measured CO<sub>2</sub> production. Furthermore, the  $r_{Acetone,T}$  can be obtained with the  $r_{Acetone,g}$  and the  $(1 + K'_{acetone})$  factor. This factor accounts for the acetone adsorbed [32], as shown in the following equations:

$$r_{Acetone,T} = (1 + K'_{acetone}) r_{Acetone,g} \quad (15)$$

$$K'_{Acetone} = \frac{K^A_{Acetone} W Q_{Acetone,max}}{V} \quad (16)$$

where  $W$  is the photocatalyst weight in g and  $V$  is the volume of the reactor.

#### 4.4.2. Quantum yields for TiO<sub>2</sub>-SC and TiO<sub>2</sub>-AAS-ASC

On the basis of the procedure discussed in Section 4.4, Quantum Yields were calculated for the acetone photodegradation in the Photo-CREC-Air Reactor at different initial concentrations. Fig. 17 compares the QYs obtained for the acetone photodegradation using the TiO<sub>2</sub>-SC and TiO<sub>2</sub>-AAS-ASC meshes.

Fig. 17 shows that for both TiO<sub>2</sub> immobilized meshes, the Quantum Yields consistently reach a 50–60% maximum level. QYs increase first and decrease progressively later with irradiation time. It is assumed that the available  $\bullet OH$  radicals first react with acetone molecules. Some of these steps lead to complete mineralization while others lead to the formation of intermediates such as acetaldehyde. Thus, the photocatalytic conversion of acetone in air involves both complete acetone mineralization (CO<sub>2</sub> formation) and partial acetone oxidation to acetaldehyde. As a result, the first stages of photoconversion are influenced by  $\bullet OH$  oxidizing both the acetone and the more reactive acetaldehyde. This explains the modest initial increase in QYs. Following this irradiation period, QYs decrease progressively given the simultaneous reduction of both

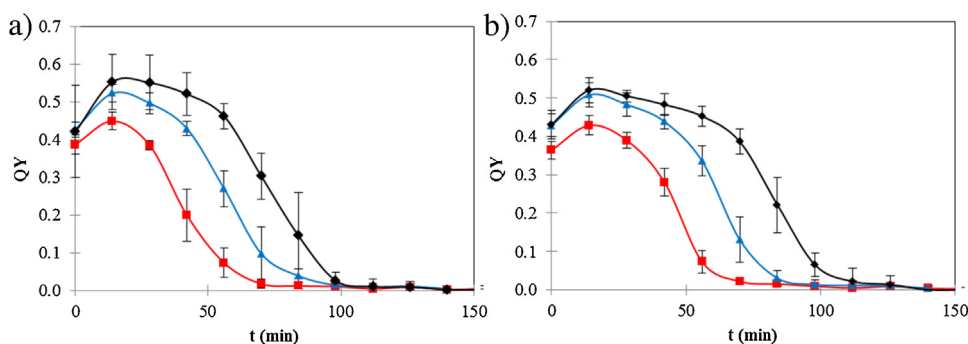


**Fig. 17.** Calculated QYs during the Photocatalytic Degradation of Acetone Using Immobilized: (a) TiO<sub>2</sub>-SC and (b) TiO<sub>2</sub>-AAS-ASC. Three initial concentrations were considered: 25 (red squares), 37 (blue triangles) and 50 μmol/L (black diamonds). (For interpretation of the references to colour in this figure legend, the reader is referred to the web version of this article.).

acetone and acetaldehyde concentrations, with all this leading to the complete mineralization of organic species.

One can mention that the observed changes in chemical species with irradiation time are the result of the so-called “series-parallel” reaction network [51]. This is the case given the unavoidable photon density differences in various TiO<sub>2</sub> immobilized mesh locations in Photo-CREC-Air when using the TiO<sub>2</sub>-SC and TiO<sub>2</sub>-AAS-ASC. One should also notice that the data reported in the present study, is also valuable to clarify the magnitude of QY values previously reported by our research group as exceeding 100% [32]. It is proven in the present study, that the QYs for TiO<sub>2</sub>-SC and TiO<sub>2</sub>-AAS-ASC meshes in the Photo-CREC-Air Reactor while showing excellent performance remain in the 55–56% range.

Furthermore and to complete the review on quantum efficiencies, a Quantum Efficiency ( $\eta_w$ ) factor based on the unit weight of the photocatalyst is considered:

$$\eta_w = \frac{QY}{W} \quad (17)$$

Fig. 18 reports the  $\eta_w$  results as a function of the irradiation time for three initial acetone concentrations.

It can be observed that the  $\eta_w$  reaches a maximum value of 0.08 1/g when using the TiO<sub>2</sub>-SC method, while this value is 0.24 1/g or three times larger when employing the TiO<sub>2</sub>-AAS-ASC technique. This demonstrates that the TiO<sub>2</sub>-AAS-ASC provides a mesh with more efficient photocatalyst utilization.

Figs. 19a and 19b schematize the utilization of photons when using both TiO<sub>2</sub>-AAS-ASC and TiO<sub>2</sub>-SC meshes. One can see that the more homogeneous TiO<sub>2</sub> distribution and limited particle agglomeration on the TiO<sub>2</sub>-AAS-ASC mesh allows for limited photocatalyst particle exposed areas with higher radiation density. Therefore, and as a result, one can explain the higher rates of •OH radicals available per unit photocatalyst weight which are observed when using the TiO<sub>2</sub>-AAS-ASC method.

Thus, one can see that once the 6–10 μm coating thickness is reached, a close to complete utilization of irradiated photons is accomplished. An extra TiO<sub>2</sub> thickness on the mesh as in TiO<sub>2</sub>-SC, does not contribute to photocatalytic conversion.

Furthermore, one can also argue that the  $\eta_w$  obtained in the present study compares favorably with the so called optimum  $\eta_w$  calculated as follows:

$$\eta_{w, optimum} = \frac{QY_{max}}{A_c L_{opt} \rho_{TiO_2} (1 - \varepsilon)} = 0.4 g^{-1} \quad (18)$$

where the  $QY_{max}$  is the maximum Quantum Yield reached in the acetone photodegradation,  $A_c$  accounts for the area of TiO<sub>2</sub> coated mesh (cm<sup>2</sup>),  $L_{opt}$  states for the optimum thickness for maximum photon utilization (cm),  $\rho_{TiO_2}$  is the density of the TiO<sub>2</sub> (g/cm<sup>3</sup>) and  $\varepsilon$  accounts for the coating porosity (0.5). The  $\eta_w$  optimum corre-

sponds to an ideal  $\eta_w$  value where the reaction rate of acetone is the highest and the thickness of the film is constant in every point of the mesh. In the specific case of a QY of 0.52, as shown in Fig. 17, this case yields to a  $\eta_w$  optimum equals to 0.4 g<sup>-1</sup>. This value is close to the best  $\eta_w$  of 0.24 g<sup>-1</sup>, which observed experimentally and reported in Fig. 18.

As a result, one can conclude that the TiO<sub>2</sub>-AAS-ASC leads to a TiO<sub>2</sub> immobilized coating with a performance close to the expected optimum values.

## 5. Conclusions

- Photocatalyst immobilization on a stainless steel mesh for a scaled up Photo-CREC-Air Reactor requires special coating methods. This is needed to achieve stable and highly performing TiO<sub>2</sub> meshes.
- Air assisted spray in conjunction with an automatized spinning coating method (TiO<sub>2</sub>-AAS-ASC) provides a uniform and stable TiO<sub>2</sub> particle coating.
- The TiO<sub>2</sub>-AAS-ASC coated mesh evaluated in a scaled up 55.1 L Photo-CREC-Air Reactor displayed high photoactivity for the photoconversion of acetone in air.
- Quantum Yields calculated in this unit, using consumed •OH radical groups and absorbed photons give 0.4–0.5 high performance values.
- Quantum Yields per unit weight of photocatalyst provide three times larger values for the TiO<sub>2</sub>-AAS-ASC mesh than when using the TiO<sub>2</sub>-SCM mesh.
- Gravimetric methods as well as SEM, show a TiO<sub>2</sub>-AAS-ASC coating with limited particle agglomeration (6–10 μm thickness for 1 wt% TiO<sub>2</sub>). This limited layer thickness is considered a close to optimum one, allowing complete absorption of photons on a coated mesh.

## Acknowledgments

The authors acknowledge the financial support from the Natural Sciences and Engineering Research Council of Canada (NSERC). C.S.L-V expresses her gratitude to The Consejo Nacional de Ciencia y Tecnología (CONACyT), México, for the scholarship (N 217085) awarded for the development of her Ph.D. program at the University of Western Ontario. C.S.L-V also thanks the Secretaria de Gobernación Pública (SEP), México, for the supplementary scholarship “Beca Complemento” (N 4351).

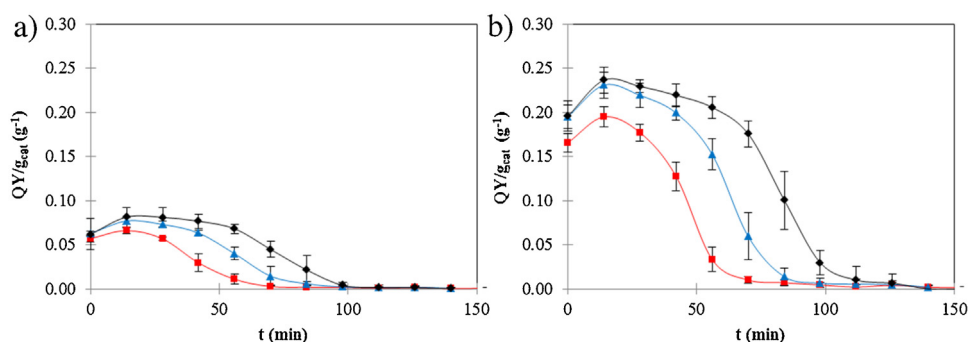


**Fig. 18.** Calculated  $\eta_w$  during the Photocatalytic Degradation of Acetone using Immobilized: (a)  $\text{TiO}_2$ -SC and (b)  $\text{TiO}_2$ -AAS-ASC. Three initial concentrations were considered: 25  $\mu\text{mol/L}$  (red squares), 37  $\mu\text{mol/L}$  (blue triangles) and 50  $\mu\text{mol/L}$  (black diamonds). (For interpretation of the references to colour in this figure legend, the reader is referred to the web version of this article.)

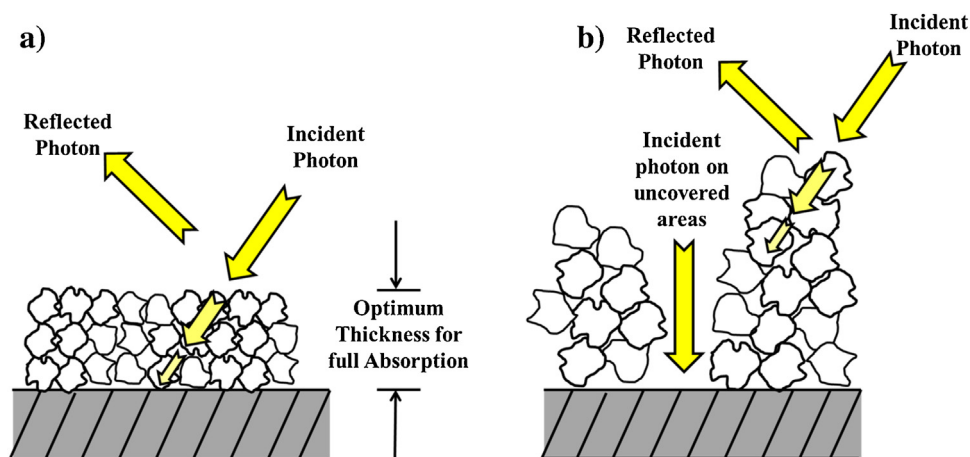


**Fig. 19.** Schematic Representation of the Particle Agglomeration and the Utilization of Photons on the  $\text{TiO}_2$  Coatings: (a)  $\text{TiO}_2$ -AAS-ASC and (b)  $\text{TiO}_2$ -SC.

## Appendix A. Spectral intensity and radiation distribution of the UV lamps

### Spectral intensity and radiation distribution of the UV lamps

A polychromatic EiKO Global Lamp was used in the present study. Fig. A1 shows the distribution of spectral emitted intensity in the 325 nm to 410 nm range with a radiation peak at 350 nm. Given that only photons with a wavelength smaller than 368 nm activate  $\text{TiO}_2$ , only 94% of the photons emitted by this lamp activate the  $\text{TiO}_2$  (grey shaded area in Fig. A1) [52]. One should also note that consistent with the data of Fig. A1, only the fraction of absorbed photons

with wavelengths below 386 nm (gray area) shall be used in the Quantum Yield calculations, with this being in agreement with Eq. (4).

Fig. A2 reports the measurements of radiation distribution in the Photo-CREC-Air reactor. These measurements were considered to calculate the total absorbed radiation through Eq. (2) and subsequently to evaluate the quantum yield with Eq. (1).

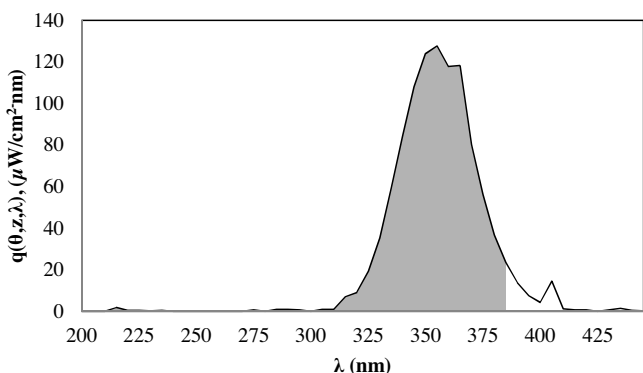


**Fig. A1.** Spectral Intensity of a Polychromatic EiKO Global UV Lamp.

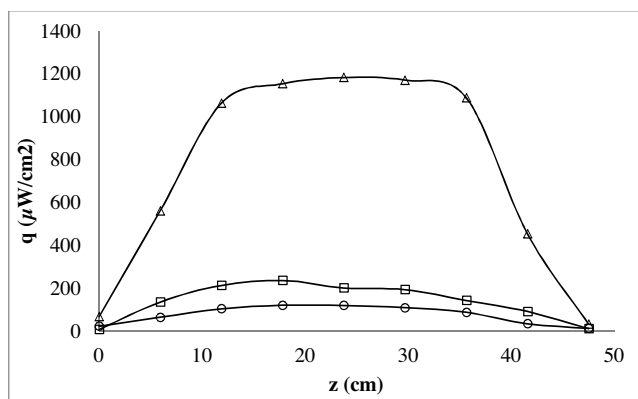


**Fig. A2.** Radiation Distribution along  $z$  Axes in the Photo-CREC-Air Reactor. Three measurement locations were considered: (a) Incident radiation on the  $\text{TiO}_2$  immobilized mesh  $\Delta$ , (b) Transmitted radiation through the mesh  $\square$  and (c) Reflected radiation by the mesh  $\circ$ .



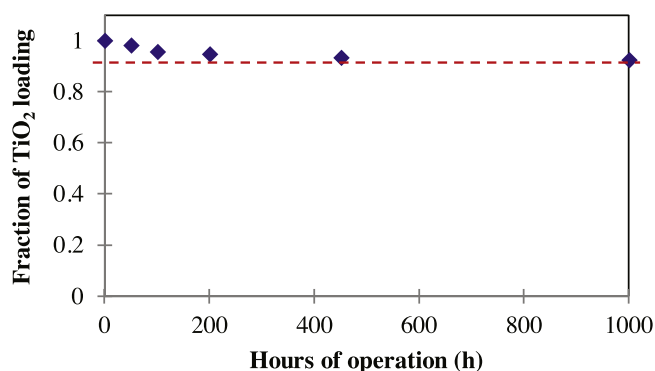


**Fig. B1.** Changes of TiO<sub>2</sub> Loading with a TiO<sub>2</sub>-AAS-ASC Mesh during 1000 h of Operation.

## Appendix B. Stability of the immobilized TiO<sub>2</sub> using the TiO<sub>2</sub>-AAS-ASC method

### Stability of the immobilized TiO<sub>2</sub> using the TiO<sub>2</sub>-AAS-ASC method

Fig. B1 reports the loading stability of the immobilized photocatalyst prepared using the TiO<sub>2</sub>-AAS-ASC method. One can notice that total TiO<sub>2</sub> losses are lower than 10 wt% after 1000 h of operation. One can also observe that these particle losses occur mainly during the first 100 h. After this initial period, the TiO<sub>2</sub> weight remains essentially unchanged within 2%.

## References

- [1] S. Aguado, A.C. Polo, Ma. P. Bernal, J.N. Coronas, J. Santamaría, J. Membr. Sci. 240 (2004) 159–166.
- [2] B.J. Finlayson-Pitts, J.N. Pitts Jr., Chemistry of the Upper and Lower Atmosphere, Academic Press, San Diego, 2000, pp. 844–870.
- [3] M. Hulin, M. Simoni, G. Viegi, I. Annesi-Maesano, Eur. Respir. J. 40 (2012) 1033–1045.
- [4] WHO, Monitoring Ambient Air Quality for Health Impact Assessment, in: World Health Organization Regional Office for Europe (Ed.), WHO Regional Publications, Copenhagen, 1999.
- [5] U.S. Environmental Protection Agency, Assessment and Control of Indoor Air Pollution, In: I.A. Division (Ed.), Washington D.C. (1989) pp. 4–14.
- [6] H. de Lasa, B. Serrano, M. Salaices, Photocatalytic Reaction Engineering, Springer, US, 2005, pp. 1–15.
- [7] D.T. Tompkins, B.J. Lawnicki, W.A. Zeltner, M.A. Anderson, Ashrae Trans. 111 (2005) 60–84.
- [8] Z. Han, V.W. Chang, L. Zhang, M.S. Tse, O.K. Tan, L.M. Hildemann, Aerosol Air Qual. Res. 12 (2012) 1327–1335.
- [9] W. Wang, J. Yu, Q. Xiang, B. Cheng, Appl. Catal. B: Environ. 119–120 (2012) 109–116.
- [10] L. Lopez, W.A. Daoud, D. Dutta, B.C. Panther, T.W. Turney, Appl. Surf. Sci. 265 (2013) 162–168.
- [11] H. de Lasa, B. Serrano, M. Salaices, Photocatalytic Reaction Engineering, Springer, US, 2005, pp. 119–131.
- [12] M. Bettoni, P. Candori, S. Falcinelli, F. Marmottini, S. Meniconi, C. Rol, G.V. Sebastiani, J. Photochem. Photobiol. A: Chem. 268 (2013) 1–6.
- [13] H. Kisch, D. Bahnemann, J. Phys. Chem. Lett. 6 (2015) 1907–1910.
- [14] N. Serpone, J. Photochem. Photobiol. A: Chem. 104 (1997) 1–12.
- [15] L. Zhang, W.A. Anderson, Chem. Eng. J. 218 (2013) 247–252.
- [16] J.M. Garcia-Hernandez, B.S. Rosales, H. de Lasa, Chem. Eng. J. 165 (2010) 891–901.
- [17] C.A. Arancibia-Bulnes, A.E. Jiménez, C.A. Estrada, Adv. Chem. Eng. 36 (2009) 185–227.
- [18] M.M. Ballari, J. Carballada, R.I. Minen, F. Salvadores, H.J.H. Brouwers, O.M. Alfano, A.E. Cassano, Process Saf. Environ. Prot. 101 (2016) 124–133.
- [19] M.J. Muñoz-Batista, A. Kubacka, A.B. Hungria, M. Fernández-García, J. Catal. 330 (2015) 154–166.
- [20] A.Y. Shan, T.I.M. Ghazi, S.A. Rashid, Appl. Catal. A: Gen. 389 (2010) 1–8.
- [21] M. Bestetti, D. Sacco, M.F. Brunella, S. Franz, R. Amadelli, L. Samiolo, Mater. Chem. Phys. 124 (2010) 1225–1231.
- [22] C. Giolli, F. Borgioli, A. Credi, A.D. Fabio, A. Fossati, M.M. Miranda, S. Parmeggiani, G. Rizzi, A. Scrivani, S. Troglia, A. Tolstoguzov, A. Zoppi, U. Bardi, Surf. Coat. Technol. 202 (2007) 13–22.
- [23] D.J. Kim, J.Y. Kang, K.S. Kim, Adv. Powder Technol. 21 (2010) 136–140.
- [24] A. Krämer, C. Kunz, S. Gräf, F.A. Müller, Appl. Surf. Sci. 353 (2015) 1046–1051.
- [25] D.Y. Lee, J.T. Kim, J.H. Park, Y.H. Kim, I.K. Lee, M.H. Lee, B.Y. Kim, Curr. Appl. Phys. 13 (2013) 1301–1305.
- [26] H. Maleki-Ghaleh, M. Shahzadeh, S.A. Hoseiniazadeh, A. Arabi, E. Aghaie, M.H. Siadati, Mater. Lett. 169 (2016) 140–143.
- [27] H.D. Traid, M.L. Vera, A.E. Ares, M.I. Litter, Procedia Mater. Sci. 9 (2015) 619–626.
- [28] S.W. Verbruggen, S. Deng, M. Kurttepli, D.J. Cott, P.M. Vereecken, S. Bals, J.A. Martens, C. Detavernier, S. Lenaerts, Appl. Catal. B: Environ. 160–161 (2014) 204–210.
- [29] Z. Zhao, J. Sun, G. Zhang, L. Bai, J. Alloys Compd. 652 (2015) 307–312.
- [30] A. Šuligoj, U.L. Štangar, A. Ristič, M. Mazaj, D. Verhovšek, N.N. Tušar, Appl. Catal. B: Environ. 184 (2016) 119–131.
- [31] H. Ibrahim, H. de Lasa, Ind. Eng. Chem. Res. 38 (1999) 3211–3217.
- [32] J.M. Garcia-Hernandez, B. Serrano-Rosales, H. de Lasa, Ind. Eng. Chem. Res. 51 (2012) 5715–5727.
- [33] H. Ibrahim, H. de Lasa, Appl. Catal. B: Environ. 38 (2002) 201–213.
- [34] J.M. Garcia-Hernandez, Photocatalytic Reactors for Air Treatment: Energy Efficiencies and Kinetic Modeling, Chemical and Biochemical Engineering, University of Western Ontario, London, ON, Canada, 2012.
- [35] H. Ibrahim, H. de Lasa, Chem. Eng. Sci. 58 (2003) 943–949.
- [36] F. Iskandar, L. Gradon, K. Okuyama, J. Colloid Interface Sci. 265 (2003) 296–303.
- [37] K. Okuyama, I. Wuled Lenggoro, Chem. Eng. Sci. 58 (2003) 537–547.
- [38] X. Li, N. Anton, C. Arpagaus, F. Belleiteix, T.F. Vandamme, J. Controlled Release 147 (2010) 304–310.
- [39] C.H. Chen, E.M. Kelder, J. Schoonman, Thin Solid Films 342 (1999) 35–41.
- [40] X.Z. Li, H. Liu, L.F. Cheng, H.J. Tong, Environ. Sci. Technol. 37 (2003) 3989–3994.
- [41] K. Fujihara, A. Kumar, R. Jose, S. Ramakrishna, S. Uchida, Nanotechnology 18 (2007) 365709.
- [42] M. Momeni, F. Golestani-Fard, H. Saghafian, N. Barati, A. Khanahmadi, Appl. Surf. Sci. 357 Part B (2015) 1902–1910.
- [43] A. Conde-Gallardo, M. Guerrero, N. Castillo, A.B. Soto, R. Fragoso, J.G. Cabañas-Moreno, Thin Solid Films 473 (2005) 68–73.
- [44] J.A. Byrne, B.R. Eggins, N.M.D. Brown, B. McKinney, M. Rouse, Appl. Catal. B: Environ. 17 (1998) 25–36.
- [45] D.S. Jung, T.H. Hwang, S.B. Park, J.W. Choi, Nano Lett. 13 (2013) 2092–2097.
- [46] S. Romero-Vargas Castrillón, H. de Lasa, Ind. Eng. Chem. Res. 46 (2007) 5867–5880.
- [47] J. Peral, D.F. Ollis, J. Catal. 136 (1992) 554–565.
- [48] W.A. Jacoby, D.M. Blake, R.D. Noble, C.A. Koval, J. Catal. 157 (1995) 87–96.
- [49] C.L. Bianchi, S. Gatto, C. Pirola, A. Naldoni, A. Di Michele, G. Cerrato, V. Crocellà, V. Capucci, Appl. Catal. B: Environ. 146 (2014) 123–130.
- [50] B. Hauchecorne, S. Lenaerts, J. Photochem. Photobiol. C: Photochem. Rev. 14 (2013) 72–85.
- [51] A. Ortiz-Gomez, B. Serrano-Rosales, M. Salaices, H. de Lasa, Ind. Eng. Chem. Res. 46 (2007) 7394–7409.
- [52] R. Thiruvengatachari, S. Vigneswaran, I.S. Moon, Korean J. Chem. Eng. 25 (2008) 64–72.